A&A 571, A34 (2014)
DOI: 10.1051/0004-6361/201424791

Astronomy & Astrophysics

The space density of Compton-thick AGN at $z \approx 0.8$ in the zCOSMOS-Bright Survey

C. Vignali[1,2], M. Mignoli[2], R. Gilli[2], A. Comastri[2], K. Iwasawa[3], G. Zamorani[2], V. Mainieri[4], and A. Bongiorno[5]

[1] Dipartimento di Fisica e Astronomia, Università degli Studi di Bologna, Viale Berti Pichat 6/2, 40127 Bologna, Italy
e-mail: cristian.vignali@unibo.it
[2] INAF – Osservatorio Astronomico di Bologna, Via Ranzani 1, 40127 Bologna, Italy
[3] ICREA and Institut de Ciències del Cosmos (ICC), Universitat de Barcelona (IEEC-UB), Martí i Franquès 1, 08028 Barcelona, Spain
[4] European Southern Observatory, Karl-Schwarzschild-Straβe 2, 85748 Garching, Germany
[5] INAF – Osservatorio Astronomico di Roma, Via Frascati 33, 00040 Monteporzio Catone, Roma, Italy

Received 11 August 2014 / Accepted 17 September 2014

ABSTRACT

Context. The obscured accretion phase in black hole growth is a crucial ingredient in many models linking the active galactic nuclei (AGN) activity with the evolution of their host galaxy. At present, a complete census of obscured AGN is still missing, although several attempts in this direction have been carried out recently, mostly in the hard X-rays and at mid-infrared wavelengths.

Aims. The purpose of this work is to assess whether the [Ne V] emission line at 3426 Å can reliably pick up obscured AGN up to $z \approx 1$ by assuming that it is a reliable proxy of the intrinsic AGN luminosity and using moderately deep X-ray data to characterize the amount of obscuration.

Methods. A sample of 69 narrow-line (Type 2) AGN at $z \approx 0.65$–1.20 were selected from the 20k-zCOSMOS Bright galaxy sample on the basis of the presence of the [Ne V]3426 Å emission. The X-ray properties of these galaxies were then derived using the *Chandra*-COSMOS coverage of the field; the X-ray-to-[Ne V] flux ratio, coupled with X-ray spectral and stacking analyses, was then used to infer whether Compton-thin or Compton-thick absorption is present in these sources. Then the [Ne V] luminosity function was computed to estimate the space density of Compton-thick AGN at $z \approx 0.8$.

Results. Twenty-three sources were detected by *Chandra*, and their properties are consistent with moderate obscuration (on average, ≈a few $\times 10^{22}$ cm^{-2}). The X-ray properties of the remaining 46 X-ray undetected Type 2 AGN (among which we expect to find the most heavily obscured objects) were derived using X-ray stacking analysis. Current data, supported by Monte Carlo simulations, indicate that a fraction as high as ≈40% of the present sample is likely to be Compton thick. The space density of Compton-thick AGN with $\log L_{2-10\ \mathrm{keV}} > 43.5$ at $z = 0.83$ is $\Phi_{\mathrm{Thick}} = (9.1 \pm 2.1) \times 10^{-6}$ Mpc^{-3}, in good agreement with both X-ray background model expectations and the previously measured space density for objects in a similar redshift and luminosity range. We regard our selection technique for Compton-thick AGN as clean but not complete, since even a mild extinction in the narrow-line region can suppress [Ne V] emission. Therefore, our estimate of their space density should be considered as a lower limit.

Key words. galaxies: nuclei – quasars: emission lines – quasars: general – X-rays: galaxies – X-rays: general

1. Introduction

The existence of a close link between super massive black holes (SMBHs) and their host galaxies has found support in many works over the last twenty years, starting from the seminal paper by Kormendy & Richstone (1995). Several relations in the local Universe between the mass of the black holes and the properties of the host galaxies (e.g., their velocity dispersion; Gebhardt et al. 2000; Ferrarese & Merritt 2000) are signatures of this connection. Most active galactic nuclei (AGN)-galaxy co-evolution models predict the existence of a dust-enshrouded phase characterized by rapid SMBH growth and active star formation, largely triggered by multiple galaxy mergers and encounters (e.g., Silk & Rees 1998; Di Matteo et al. 2005; Menci et al. 2008; Zubovas & King 2012; Lamastra et al. 2013). This phase is associated with obscured AGN growth in strongly star-forming galaxies, as already shown a decade ago by Alexander et al. (2005) using sub-millimeter selection and deep X-ray data. Then massive AGN-driven outflows blow away most of the cold gas reservoir; the AGN become unobscured (i.e., Type 1) and, when the phase of significant nuclear accretion is over because of the limited amount of remaining available gas, a population of what are known as red-and-dead gas-poor elliptical galaxies is what is left (e.g., Hopkins et al. 2008; Cattaneo et al. 2009). If, on the one hand, this scenario seems to provide a valid explanation for the most luminous and massive systems, for which a large fraction of the mass is assembled in relatively short periods (≈10−100 Myr) of intense nuclear and star-forming activity, on the other hand the bulk of galaxies and SMBHs are likely to grow their mass in a secular (i.e., smooth) mode over timescales of Gyrs (e.g., Daddi et al. 2007a; Hickox et al. 2009; Villforth et al. 2014, and references therein).

Although there is a large quantity of evidence for feedback processes in terms of outflows in molecular and neutral/ionized gas, at both low and high redshift (e.g., Nesvadba et al. 2008; Feruglio et al. 2010; Maiolino et al. 2012; Harrison et al. 2012, 2014; Cicone et al. 2014; Brusa et al. 2014), including signatures in the X-ray band (e.g., Chartas et al. 2002; Tombesi et al. 2012, and references therein), this picture still needs to be confirmed in most of its aspects. In particular, we need to

investigate the crucial phase during which large amounts of gas are funneled to the center, thus inducing both obscured accretion and star formation (e.g., Treister et al. 2010). Type 2 (obscured) AGN are evidence of and, at the same time, main actors in this phase; finding them across cosmic time is therefore crucial to place constraints on AGN vs. galaxy co-evolution models (see, e.g., the reviews by Merloni & Heinz 2013 and Vignali 2014) as well as on X-ray background synthesis models (XRB; e.g., Gilli et al. 2007; Ballantyne 2009; Treister et al. 2009; Akylas et al. 2012; Shi et al. 2013; see also Moretti et al. 2012).

A complete census of absorbed AGN, especially of the most heavily obscured (called Compton thick, having column densities above 1.5×10^{24} cm^{-2}; see Comastri 2004 for a review) up to high redshift cannot be achieved using either a single selection or a single observing-band method. Although the hard X-ray band up to ≈100–150 keV is potentially appropriate to provide an almost unbiased census of obscured AGN, since both Compton-thin (with $N_{\rm H} < 1.5 \times 10^{24}$ cm^{-2}) and Compton-thick AGN (at least the sources having column densities up to $\approx10^{25}$ cm^{-2}) can be detected by hard X-ray instruments, the sensitivity of *Swift*/BAT and INTEGRAL/IBIS surveys ($\approx10^{-11}$ erg cm^{-2} s^{-1}; e.g., Tueller et al. 2008; Beckmann et al. 2009; Burlon et al. 2011; Ajello et al. 2012; Vasudevan et al. 2013) is such to limit this kind of investigations to the local Universe. Interesting prospects might come from the much higher sensitivity (a factor of ≈100) hard X-ray imaging instrument onboard NuSTAR (e.g., Alexander et al. 2013; Lansbury et al. 2014).

A proper evaluation of obscured AGN at higher redshifts and at fainter X-ray fluxes requires deep X-ray surveys with *Chandra* and *XMM-Newton* (e.g., Tozzi et al. 2006; Georgantopoulos et al. 2009, 2013; Comastri et al. 2011; Feruglio et al. 2011; Gilli et al. 2011, 2014; Iwasawa et al. 2012a; Brightman & Ueda 2012; Vito et al. 2013; Buchner et al. 2014; Brightman et al. 2014). However, even the deepest X-ray exposures currently available miss a significant number of very obscured AGN, especially the most heavily Compton-thick AGN at low-medium redshift (because of the energy bandpass, poor counting statistics and sensitivity), hence a not negligible fraction of the accretion power in the Universe, and convey the idea that a multi-wavelength approach to the search for obscured AGN is mandatory.

The availability of deep radio, optical and mid-infrared (mid-IR) data has recently allowed the definition of complementary methods to pick up obscured AGN up to high redshifts. In particular, sources with weak emission in the optical band (due to dust extinction) and relatively bright mid-IR emission (due to the disk emission being thermally reprocessed by the AGN torus) can be considered good obscured AGN candidates (e.g., Martínez-Sansigre et al. 2005; Houck et al. 2005; Weedman et al. 2006; Dey et al. 2008), unless a significant contribution to the mid-IR comes from star formation processes (PAH features and continuum emission). This selection of obscured AGN, albeit not complete, represents a step forward with respect to mid-IR color-color diagrams, where separating heavily obscured AGN from the remaining AGN populations is not trivial (e.g., Lacy et al. 2004, 2013; Stern et al. 2005; Donley et al. 2012; Castelló-Mor et al. 2013; Mateos et al. 2013). However, the selection of obscured AGN by means of long-wavelength data needs to be corroborated by X-ray information, as plenty of works have shown in the last decade (e.g., Polletta et al. 2006; Fiore et al. 2008; Lanzuisi et al. 2009; Severgnini et al. 2012; Del Moro et al. 2013). This observational approach has led many authors to place constraints, for the first time, to the space density of Compton-thick AGN at high redshifts ($z \approx 2$–3; Daddi et al. 2007b; Fiore et al. 2009; Bauer et al. 2010; Alexander et al. 2011).

Obscured AGN can be selected also on the basis of narrow, high-ionization emission lines, like [O III]5007 Å and [Ne V]3426 Å. These lines are produced in the narrow-line region (NLR), so they do not suffer from the effects of attenuation ascribed to the torus obscuring material (although some extinction within the NLR may be present). As such, these lines can be considered good proxies of the nuclear emission from the AGN. Previous works have shown that coupling AGN selection in one of these lines with X-ray observations may be effective in finding highly reliable Compton-thick AGN candidates (e.g., Vignali et al. 2006, 2010; Ptak et al. 2006; LaMassa et al. 2009; Lamastra et al. 2009; Gilli et al. 2010, hereafter G10; Jia et al. 2013; but see also Trouille & Barger 2010). Once again, X-ray information is crucial to infer the nature of such sources, at least on a statistical ground, with additional enlightening indications coming from the mid-IR emission (e.g., Vignali et al. 2010; Goulding et al. 2011; see also Gandhi et al. 2009).

In this paper we present the X-ray properties of a sample of Type 2 AGN selected from the 20k-zCOSMOS Bright survey (Mignoli et al. 2013, hereafter M13). The optical selection and X-ray (mostly *Chandra*) coverage are shown in Sect. 2. Results from X-ray spectroscopy and stacking analyses are reported in Sect. 3, along with the estimated fraction of Compton-thick AGN. Their space density at $z \approx 0.8$ is then computed in Sect. 4, where current results are also compared with expectations based on AGN synthesis models of the XRB. Conclusions are then reported in Sect. 5.

Hereafter we adopt a cosmology with $H_0 = 70$ km s^{-1} Mpc^{-1}, $\Omega_{\rm M} = 0.3$ and $\Omega_\Lambda = 0.7$.

2. The sample: optical selection and *Chandra* coverage

The selection of the [Ne V] Type 2 AGN sample has been extensively described and discussed in M13. In the following, we will report on the main issues related to the optical selection process, the X-ray coverage, the fraction of X-ray detections, and the X-ray flux estimates needed to place sources in the *X*/NeV flux ratio diagnostic histogram (G10).

Type 2 AGN were selected from the zCOSMOS spectroscopic survey (Lilly et al. 2007, 2009), which was designed to observe ≈20 000 galaxies at *I*-band magnitudes brighter than 22.5 over the entire ≈2 square degree Cosmic Evolution Survey (COSMOS) field (Scoville et al. 2007), at a medium resolution ($R \approx 600$) and in the 5500–9700 Å spectral range with the VLT instrument VIMOS. Hereafter, this spectroscopic survey will be referred to as the 20k-zCOSMOS Bright survey.

Ninety-four Type 2 AGN were selected from the 20k-zCOSMOS survey in the redshift range ≈0.65–1.20. The lower redshift boundary guarantees that both [Ne V]3346 Å and [Ne V]3426 Å emission lines fall within the spectral coverage; the choice of the upper boundary is due to the strong fringing of VIMOS spectra at long wavelengths, which makes the process of line detection more difficult and less reliable. The Type 2 classification was based on accurate analysis of all of the optical spectra, showing only narrow features. The presence of significant emission from broad emission-line components is ruled out, as clearly shown in the composite spectrum of the Type 2 AGN sample in M13 (see their Fig. 2). The rest-frame equivalent width (EW) of the [Ne V] emission line spans the range ≈2–35Å, with a median value of ≈8 Å.

Seventy-one of these [Ne V]-selected Type 2 AGN fall in the *Chandra*-COSMOS mosaic (≈ 0.9 square degrees). Two of these sources fall in a bad position of the mosaic and were therefore discarded. The choice of focusing on *Chandra* instead of *XMM-Newton* to derive the X-ray properties of this sample is due to the typically deeper exposure in the *Chandra* mosaic (≈160 ks over the inner 0.45 square degrees – thus reaching fainter flux limits than XMM-COSMOS by a factor of ≈3.5 – and an outer region of ≈0.4 square degrees with an effective exposure of up to ≈80 ks; see Puccetti et al. 2009; Elvis et al. 2009; Civano et al. 2012, hereafter C12), and to its better performances when investigation concerns X-ray faint sources. The low and "smooth" background level of *Chandra* observations is also an important ingredient for stacking analyses.

Twenty-three [Ne V]-selected Type 2 AGN were detected by *Chandra* (see Table 1) within 1.2″ from the optical position. The median displacement between the X-ray and the optical counterpart, 0.46″, and the maximum likelihood technique presented by C12 assure the reliability of the associations. We have visually inspected the four sources with a counterpart at a distance larger than 1 arcsec and found they are good matches.

To characterize the sources in terms of obscuration, we used the *X*/NeV flux ratio diagram (as in G10), where *X* corresponds to the rest-frame 2–10 keV flux with no absorption correction, and NeV is the flux of the emission line derived from the zCOSMOS spectra after applying aperture corrections, whose median value corresponds to a factor of ≈1.5 (see Sect. 6 of M13). The rest-frame 2–10 keV band corresponds to the observed-frame ≈1–5.5 keV band. We have extracted the 23 [NeV]-selected source information from the multiple pointings of the *Chandra*-COSMOS mosaic using the procedure outlined in M13 and derived X-ray photometry in the chosen energy interval. Because of the tiles in the C-COSMOS field, every source can be observed in more than one pointing (up to six) and at different locations within the ACIS-I field of view, hence the source count distribution is characterized by different (i.e., multiple) point spread function (PSF) sizes and shapes. To properly account for these effects, we have used the ACIS EXTRACT software (Broos et al. 2010), which extracts the source counts from each observation using the 90% of the encircled energy fraction at 1.5 keV at the source position and then corrects for the chosen aperture. At this stage, counts were extracted in the rest-frame 2–10 keV for each source and divided by the effective (i.e., "vignetting-corrected") exposure time at each source position (averaged over an area of 5-arcsec radius to minimize the possible effects of small-scale fluctuations in the timemaps) to obtain a count rate. The X-ray flux has then been obtained by a simple count rate to flux conversion, assuming a powerlaw model with photon index $\Gamma = 1.4$ modified by Galactic absorption. The corresponding *X*/NeV flux ratios are plotted in Fig. 1 (red filled region).

Along with photometry, X-ray spectra were also extracted and fitted with a simple model (a powerlaw modified by Galactic absorption), because of the limited photon statistics for most of these sources (see Sect. 3.1). This X-ray spectral analysis allowed us to derive another estimate for the rest-frame 2–10 keV fluxes (see Table 1, where two *X*/NeV columns are shown, corresponding to the two methods used to derive X-ray fluxes). The *X*/NeV flux ratios corresponding to this basic X-ray spectral analysis are plotted in Fig. 1 as a blue dotted histogram. Details on the X-ray properties of these 23 Type 2 AGN are presented in Sect. 3.1.

A similar, ACIS EXTRACT-based procedure has been adopted for the X-ray photometry of the remaining 46 [Ne V]-selected Type 2 AGN with no X-ray detection in the C12 catalog (and

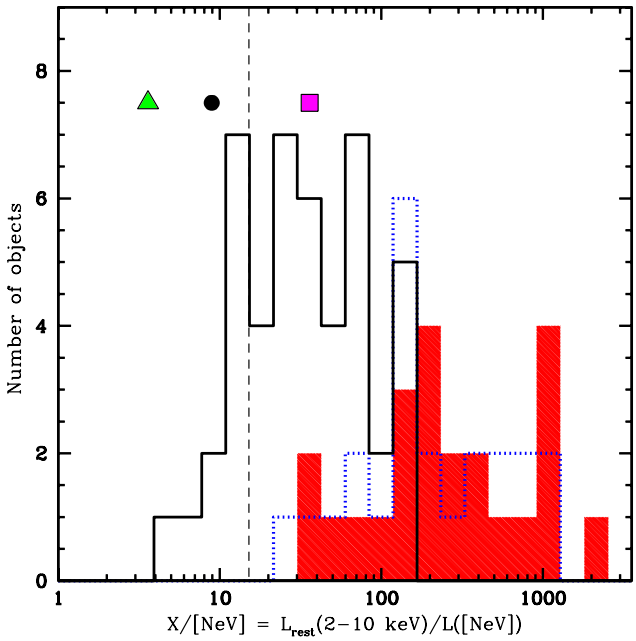

Fig. 1. Distribution of the rest-frame 2–10 keV (with no correction for absorption) to [NeV] luminosity ratio (*X*/NeV) of the 69 zCOSMOS Type 2 AGN with reliable X-ray photometry. X-ray detections are reported as either red (filled) or blue (dotted) histograms; in particular, the red histogram refers to X-ray photometry obtained from the ACIS EXTRACT analysis carried out in the rest-frame 2–10 keV band, while the blue histogram reports the X-ray flux values derived from direct X-ray spectral fitting in the same energy band (see text for details). The black histogram refers to the X-ray undetected [Ne V]-selected Type 2 AGN. The vertical dashed line shows the threshold defined by G10 for Compton-thick (leftward direction) and Compton-thin (rightward direction) sources. All of the X-ray detected sources are likely Compton thin using the *X*/NeV threshold of 15 adopted by G10. The filled symbols represent the average *X*/NeV value obtained from the X-ray stacking analysis (black circle: stack of the 46 X-ray undetected Type 2 AGN; green triangle: stack of the 22 sources with "nominal" upper limit on the *X*/NeV ratio <30; magenta square: stack of the 24 sources with "nominal" upper limit on the *X*/NeV ratio >30; see Sect. 3.2 for details). Their *y*-axis position is arbitrary.

no clear X-ray emission in the 0.5–7 keV images). To derive X-ray flux upper limits, at each source optical position counts were extracted taking into account the PSF size and shape in the observed band equivalent to the rest-frame 2–10 keV energy interval. One-sigma count upper limits have then been converted into count rates using the exposures derived from the timemaps at each source position, and count rates were then converted into X-ray flux upper limits assuming a powerlaw with photon index $\Gamma = -0.4$, which is broadly consistent with a reflection-dominated spectrum. These values were then used to derive the *X*/NeV flux ratio upper limits reported in Table 2, similarly to the analysis presented in M13. We note that Monte Carlo runs were then used to properly interpret the results obtained for the X-ray undetected Type 2 AGN given their limited photon statistics (see Sect. 3.2 for details).

The different behavior in the X-ray band between the sample of 23 X-ray detected and that of 46 X-ray undetected Type 2 AGN cannot be ascribed to a difference in the exposure time; the former sample has an average exposure of ≈120 ks, while the latter is characterized by a slightly larger exposure, ≈128 ks. Furthermore, the two samples have comparable average redshift

Table 1. List of X-ray detected [NeV]-selected Type 2 AGN.

zCOSMOS_ID	$RA_{(J2000)}$	$Dec_{(J2000)}$	z	I mag	CID	T_{Expo}	X/[NeV]	Xs/[NeV]	Ncts	$F_{2-10\ keV}$	XMMID
(1)	(2)	(3)	(4)	(5)	(6)	(7)	(8)	(9)	(10)	(11)	(12)
810378	150.467621	1.935703	0.9707	21.81	401	75.99	182.5	181.7	29	2.0	60205
812111	150.097778	1.845246	0.7106	21.18	254	146.23	162.1	136.7	55	0.5	−99
813250	149.830582	1.902132	0.7302	21.62	1019	156.12	91.4	38.5	27	0.8	−99
813287	149.820557	1.811719	0.7488	20.41	221	63.70	1057.8	428.3	61	0.6	5139
816439	150.510666	2.029207	0.8988	20.92	496	72.13	181.8	146.2	90	1.6	2387
817002	150.418167	1.976701	0.8649	20.73	381	91.29	346.3	295.0	77	2.1	2473
817871	150.248688	1.972335	0.6739	20.16	1508	159.31	37.6	62.2	12	0.5	−99
817977	150.222534	2.011670	0.9591	21.32	1169	214.06	262.8	135.2	30	0.2	−99
819469	149.893555	2.107714	0.6865	21.35	339	161.58	998.0	785.8	367	2.0	64
820695	149.580399	1.967788	0.7642	21.64	1706	36.88	69.9	..... [a]	5	.....	−99
820742	149.570389	1.990572	0.9997	21.98	173	53.45	2079.8	1007.1	79	1.5	5288
825282	150.018860	2.147779	0.9588	20.90	1126	164.75	211.5	171.7	91	1.4	54534
825838	149.907333	2.169099	0.7864	21.23	1130	124.24	252.5	158.2	43	0.3	497
826095	149.856766	2.273134	0.7640	20.62	2454	150.51	43.3	..... [a]	10	.....	364
829955	150.444427	2.369805	0.8913	21.41	717	162.04	149.3	108.9	78	0.5	172
831966	150.062149	2.455000	0.7295	20.70	110	156.57	976.1	747.3	309	1.8	99
832900	149.884171	2.338150	1.0230	21.30	456	181.28	136.9	122.8	165	2.7	413
833208	149.826523	2.396749	0.9106	22.38	503	132.04	637.8	538.4	65	1.5	5224
833510	149.768112	2.431331	0.9444	20.94	522	78.00	661.6	565.2	160	3.3	2237
833904	149.691101	2.335542	0.8643	21.67	426	73.95	354.4	349.0	43	1.3	229
837988	150.274323	2.511393	0.7034	20.72	138	73.65	1084.2	947.7	84	1.5	158
840085	149.910660	2.554670	0.7535	20.01	1230	163.37	34.1	23.7	32	0.2	5008
846478	150.015457	2.665832	1.1767	22.13	620	79.62	179.8	149.6	57	1.6	5427

Notes. (1) Identification number in the 20k-zCOSMOS Bright survey; (2) optical right ascension and (3) declination; (4) redshift from the 20k-zCOSMOS Bright spectroscopic survey; (5) I-band AB magnitude; (6) identification number according to the *Chandra*-COSMOS source catalog (C12); (7) net ("vignetting-corrected") exposure time in the *Chandra* mosaic (ks); (8) X/NeV flux ratio using X-ray aperture photometry from ACIS EXTRACT to compute the rest-frame 2–10 keV flux (see Sect. 2 for details); (9) X/NeV flux ratio using the X-ray flux from spectral fitting of the data using XSPEC; (10) number of net counts from ACIS EXTRACT in the observed ≈0.5–7 keV energy band; (11) observed-frame 2–10 keV flux (from X-ray spectral analysis, in units of 10^{-14} erg cm^{-2} s^{-1}); (12) identification ID in the XMM-COSMOS source catalog (Brusa et al. 2010; see also Cappelluti et al. 2009). −99 indicates that the source was not detected by *XMM-Newton*. [(a)] For this source, the X-ray photon statistics was not sufficient to compute a reliable X-ray flux in the rest-frame 2–10 keV band.

($z = 0.85$ vs. $z = 0.84$) and similar [Ne V] flux (3.1×10^{-17} vs. 2.8×10^{-17} erg cm^{-2} s^{-1}). Therefore, we motivate our choice of a different photon index for the count rate to flux conversion for the two samples under the hypothesis that X-ray undetected Type 2 AGN may suffer from heavier absorption than X-ray detected Type 2 AGN.

As a final remark, we note that the present sample of Type 2 AGN is far from being complete, as extensively discussed by M13. In particular, there are other ≈160 zCOSMOS galaxies in the same redshift interval having the properties of Type 2 AGN (either from optical spectroscopy or X-ray analysis or both) without the presence of [Ne V] emission. The mean optical extinction of this sample (derived from the Hβ/Hγ flux ratio, $\langle E(B-V)\rangle = 0.27$) is higher than that derived for the [Ne V]-selected Type 2 AGN discussed in this paper ($\langle E(B-V)\rangle = 0.18$); the higher extinction is likely causing the lack of appreciable [Ne V] emission in the "additional" sample of Type 2 AGN (see Fig. 6 of M13). Summarizing, the AGN selection based on [Ne V] emission can be considered clean (because of the ionization potential of this line, unambiguously ascribed to accretion power) but not complete.

3. X-ray results

3.1. X-ray detected [NeV]-selected Type 2 AGN

For the 23 X-ray detected Type 2 AGN we were able to perform a basic X-ray spectral analysis assuming a powerlaw model. The main limitation of this analysis is due to the paucity of X-ray photons available in our data. The median number of net (i.e., background-subtracted) counts is 60. Two sources have ten counts or fewer, two sources have 140–150 counts (CID = 456 and 522, according to C12 source nomenclature), and two sources have 300–350 counts (CID = 110 and 339).

On the one hand, fitting all the X-ray data together with the same model (accounting for the different redshifts and fluxes of the sources) would produce biased results, given the presence of four AGN with more than 100 counts. On the other hand, fitting all the spectra individually using unbinned data and C-statistic (Cash 1979) within XSPEC (Version 12.7.0; Arnaud 1996) would not constrain properly the X-ray spectral parameters (Γ, $N_{\rm H}$ and normalization) for most of the 23 sources. Therefore, we decided to fit the four sources with most counts using χ^2 statistics and binned data (10–15 counts per bin); the remaining spectra were "summed" to produce a rest-frame 1–10 keV stacked spectrum (with a spectral resolution of ≈0.5 keV) – following the prescriptions extensively described in Iwasawa et al. (2012a,b) – and then fitted (again, adopting the χ^2 statistics).

Errors are quoted at the 90% confidence level for one parameter of interest ($\Delta\chi^2 = 2.71$; Avni 1976). Solar abundances (from Anders & Grevesse 1989) and Galactic absorption ($N_{\rm H} = 1.7 \times 10^{20}$ cm^{-2}; Kalberla et al. 2005) were adopted in all models.

CID339 and CID110 are characterized by single powerlaws with limited absorption at the source redshift ($N_{\rm H} = 3.8^{+3.2}_{-2.8} \times 10^{21}$ cm^{-2} and $N_{\rm H} < 3.4 \times 10^{21}$ cm^{-2}, respectively, once a

Table 2. List of X-ray undetected [NeV]-selected Type 2 AGN.

zCOSMOS_ID	$RA_{(J2000)}$	$Dec_{(J2000)}$	z	I mag	T_{Expo}	X/[NeV]
(1)	(2)	(3)	(4)	(5)	(6)	(7)
804431	150.383041	1.745181	0.7020	22.06	73.97	<81.0
805117	150.220490	1.729720	0.9999	22.36	85.50	<48.6
811284	150.269028	1.891863	0.9558	22.35	191.74	<12.9
811645	150.195160	1.841540	0.8092	21.89	159.36	<29.7
811887	150.144485	1.853603	0.7297	22.25	158.61	<10.9
812193	150.080215	1.849570	0.8980	21.63	159.35	<11.6
812432	150.025848	1.926400	0.6611	20.88	160.28	<10.0
812665	149.971375	1.885972	0.7301	20.88	147.61	<37.0
812953	149.900970	1.947447	0.7742	21.45	166.61	<12.3
813366	149.803879	1.795451	0.6685	20.05	78.14	<15.1
813460	149.780212	1.826555	0.6646	22.07	79.85	<140.1
813850	149.697205	1.905195	0.6606	20.33	76.58	<118.3
814229	149.607040	1.870499	0.7618	22.47	47.41	<7.9
817886	150.244629	2.008821	0.9603	21.74	190.76	<119.9
818408	150.135941	2.120217	0.6688	20.85	222.98	<36.5
818478	150.122849	2.085841	0.8946	22.29	232.48	<48.5
819116	149.972672	2.049503	0.7150	22.00	174.97	<4.6
819306	149.929489	2.110626	0.9394	21.89	164.92	<37.6
820589	149.606232	2.062873	0.8796	20.78	71.91	<38.9
823097	150.469711	2.231583	0.8044	22.23	95.79	<41.8
823162	150.458023	2.260842	0.8489	22.07	119.31	<20.4
823537	150.380005	2.128212	0.9226	21.98	169.38	<15.0
824025	150.273239	2.273062	0.8503	21.24	161.43	<20.6
824548	150.163940	2.290950	0.7480	21.89	163.79	<6.6
824736	150.123535	2.149813	1.1427	22.23	199.43	<15.9
825958	149.884903	2.238505	0.7026	20.95	165.84	<74.1
826023	149.872528	2.162082	0.9508	21.99	151.25	<27.1
826693	149.733231	2.132358	0.6994	22.47	155.93	<138.9
826908	149.695847	2.267107	1.0246	21.46	60.92	<93.4
829551	150.525146	2.456414	0.8927	21.81	71.55	<73.9
829938	150.446548	2.366708	0.8821	21.40	163.52	<28.8
830027	150.431183	2.359476	0.9307	22.32	149.35	<29.2
831655	150.112289	2.387432	0.7567	21.68	151.48	<98.4
832252	150.013412	2.333157	0.7878	21.90	157.53	<20.7
832576	149.948395	2.449379	0.7332	21.91	194.50	<63.6
832803	149.905640	2.318273	0.9274	21.49	168.74	<23.4
832907	149.883438	2.373879	0.9608	21.65	149.44	<25.0
836868	150.477036	2.494094	0.6793	20.78	74.56	<128.5
837072	150.439438	2.543515	1.1475	22.44	55.70	<27.3
837589	150.347275	2.570119	0.9214	21.47	69.47	<41.5
839719	149.963074	2.613115	0.8916	21.64	62.41	<80.1
840744	149.772919	2.555765	0.7353	20.68	79.26	<52.4
846342	150.041229	2.634787	0.7353	20.67	73.21	<14.0
846946	149.921646	2.638877	0.7379	21.44	75.52	<47.2
847446	149.815765	2.650275	1.0273	22.24	39.18	<73.2
910023	150.491974	2.458913	0.9802	21.18	77.54	<63.9

Notes. (1) Identification number in the 20k-zCOSMOS Bright Survey; (2) optical right ascension and (3) declination; (4) redshift; (5) I-band *AB* magnitude; (6) net ("vignetting-corrected") exposure time in the *Chandra* mosaic (ks); (7) X/NeV flux ratio using X-ray aperture photometry from ACIS EXTRACT to compute the rest-frame 2–10 keV flux (see Sect. 2 for details). Only one of the sources reported above, zCOSMOS_ID = 813850, has been detected in XMM-COSMOS (XMMID = 60494, detected in the 2–8 keV band at the $\approx 4.8\sigma$ level; see Cappelluti et al. 2009; Brusa et al. 2010). We note that this source is just below the detection threshold in the C-COSMOS source catalog.

"canonical" AGN photon index $\Gamma = 1.8$ – e.g., Piconcelli et al. (2005) – is assumed; see panels (a) and (b) in Fig. 2); we note that the best-fitting Γ for the two sources ($\approx$1.6–1.7) are very close to the adopted value. An emission line at rest-frame energy $\approx$6.9 keV is tentatively detected ($\approx 2.5\sigma$) in CID339. The other two relatively bright sources, CID522 and CID456, appear more absorbed, being characterized by $\Gamma \approx 0.9 - 1.2$ if no absorption is included. Fixing the photon index to 1.8 and including obscuration in the fit produce a column density of $2.7^{+2.3}_{-2.0} \times 10^{22}$ cm^{-2} and $3.1^{+1.4}_{-1.0} \times 10^{23}$ cm^{-2}, respectively (see panels (c) and (d) in Fig. 2).

The 1–10 keV stacked spectrum of the remaining sources is characterized by a flat slope and an emission feature which, at first glance, is consistent with iron emission (see the X-ray stacked spectrum in panel (e) of Fig. 2). If no absorption is assumed, $\Gamma = 0.8 \pm 0.1$ is derived. Similarly to the sources above, the photon index was fixed to 1.8, and the derived column density is $N_{\rm H} = 2.2^{+0.6}_{-0.5} \times 10^{22}$ cm^{-2}. This column density is consistent with the broad range of X/NeV (hence absorption) encompassed by these sources (see the filled red and open blue histograms in Fig. 1, and Table 1). The emission-line energy is 6.4 ± 0.2 keV, in agreement with either neutral or mildly ionized

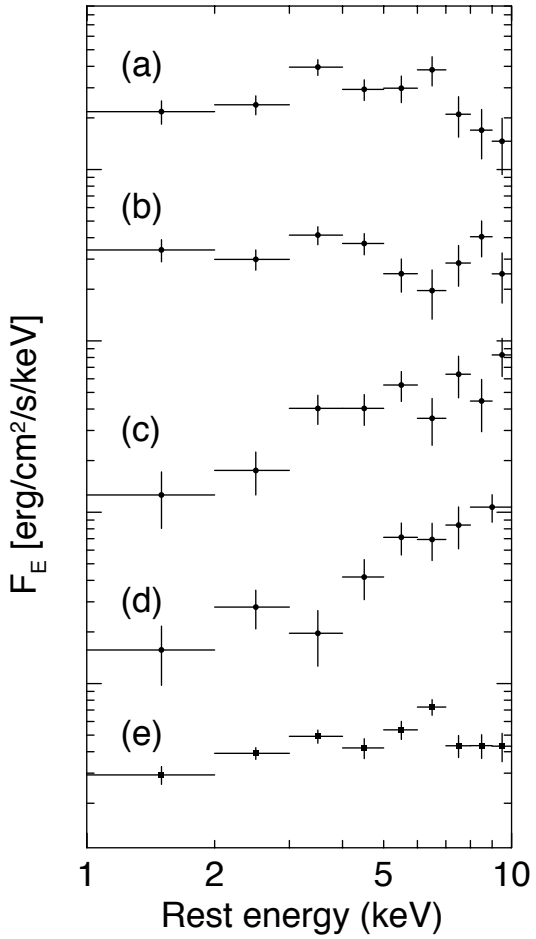

Fig. 2. Rest-frame X-ray spectra of the four Type 2 AGN with most counts (i.e., above 140 counts; CID339 **a)**, CID110 **b)**, CID522 **c)**, and CID456 **d)**), characterized by increasing absorption from top to bottom, and stacked X-ray spectrum of the 19 Type 2 AGN with limited photon statistics (panel **e)**), showing an emission line at an energy consistent with iron Kα. An emission line is also apparent in CID339. X-ray spectra are arbitrarily scaled for visual clarity.

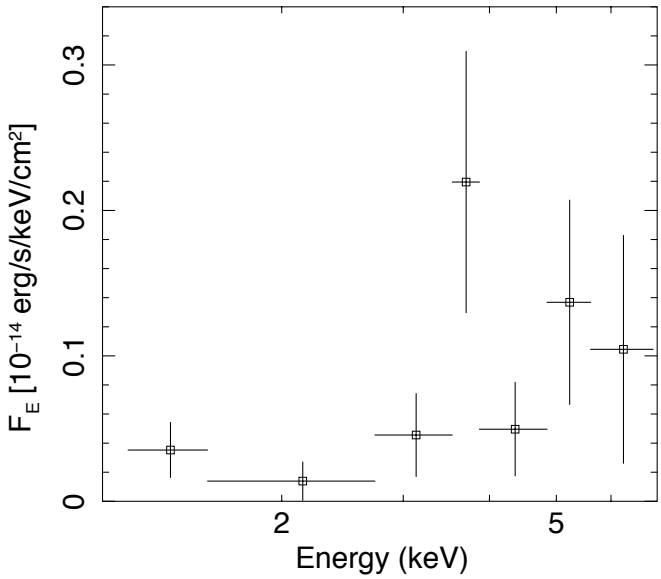

Fig. 3. Observed-frame X-ray spectrum of CID1019 (zCOSMOS_ID = 813250) at $z = 0.7302$. The flat X-ray continuum and the tentative iron Kα emission line at rest-frame energy of ≈6.4 keV are indicative of strong, likely Compton-thick absorption.

iron, and its equivalent width is $EW = 0.7 \pm 0.4$ keV. Since a typical signature of strong obscuration is the presence of a strong ($EW \gtrsim 1$ keV) FeKα emission line on top of a flat X-ray continuum (e.g., Comastri et al. 2011; Feruglio et al. 2011; Iwasawa et al. 2012a), we might interpret the EW of the iron line in the stacked spectrum as suggestive of the presence of a few sources with heavy obscuration.

The X-ray spectral results obtained from the stacked spectrum were confirmed by fitting the spectra simultaneously (i.e., all of the sources were fitted at the same time using the same spectral model, leaving the normalization of each source free to vary; here *C*-statistic is adopted). Assuming $\Gamma = 1.8$, we obtain $N_{\rm H} = (2.2 \pm 0.4) \times 10^{22}$ cm^{-2} (consistent with the analysis reported above) but the iron line does not emerge as strongly as in the stacked spectrum described above.

Among the analyzed X-ray spectra, of particular interest is the case of source CID1019, corresponding to the zCOSMOS object 813250 at $z = 0.7302$ (≈30 background-subtracted counts). A single powerlaw provides $\Gamma \approx -0.5$, which is definitely an indication of heavy absorption and is consistent with a reflection-dominated spectrum below 10 keV, despite the relatively high *X*/NeV ratio (≈40–90, see Table 1). The tentative presence of an iron Kα emission at the rest-frame energy of ≈6.4 keV with $EW \approx 1.7$ keV further supports this scenario (see the X-ray spectrum in Fig. 3).

Eighteen of the 23 Type 2 AGN were detected also by *XMM-Newton*. Typically, the signal-to-noise ratios in *Chandra* spectra are higher than in *XMM-Newton* spectra (see Mainieri et al. 2007) because of the much lower background guaranteed by the former satellite. Basic X-ray spectral analysis of *XMM-Newton* data confirms the *Chandra* results in terms of spectral properties. Interestingly, there are three sources showing X-ray flux variability by at least a factor of two, with CID1230 being a factor of ≈6 fainter in *Chandra* than in *XMM-Newton*. Unfortunately, the limited number of counts (≈30 net counts in the 0.5–7 keV band in *Chandra*, and ≈130 in *XMM-Newton* in the same energy band) prevented us from investigating the nature of this difference properly.

3.2. [NeV]-selected Type 2 AGN with no X-ray detection

Results for the sample of 46 X-ray undetected [Ne V]-selected Type 2 AGN have been obtained by X-ray stacking and *X*/NeV ratio analyses. Because of the limited photon statistics, the former approach is not highly effective in constraining the average spectral properties of the sources. The fitted photon distribution (130 counts in the observed-frame 0.5–7 keV band) is consistent with a powerlaw with $\Gamma = 0.9 \pm 0.5$, indicative of obscuration (see the rest-frame 1–10 keV spectrum in Fig. 4). The derived average flux and luminosity of this sample in the rest-frame 2–10 keV band are $\approx 2.5 \times 10^{-16}$ erg cm^{-2} s^{-1}and $\approx 8.4 \times 10^{41}$ erg s^{-1}, respectively.

A step forward in the analysis of this sample consists of placing their *X*/NeV upper limits in Fig. 1 (open histogram). At face value, 39 of these sources have upper limits below 100, i.e., consistent with column densities possibly exceeding 10^{23} cm^{-2} (see G10). Nine of these upper limits are located in the region likely populated by Compton-thick AGN (i.e., at *X*/Ne < 15; G10). The average *X*/NeV ratio for these 46 sources is 9.8 (filled circle in Fig. 1).

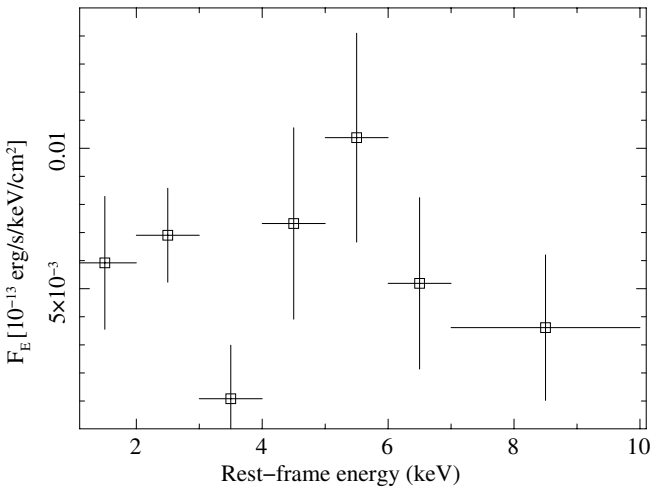

Fig. 4. Rest-frame 1–10 keV stacked spectrum of the 46 Type 2 AGN with no individual X-ray detection. The limited-quality spectrum is flat, suggestive of absorption, but apparently no significant iron Kα emission line is present ($EW < 1.5$ keV).

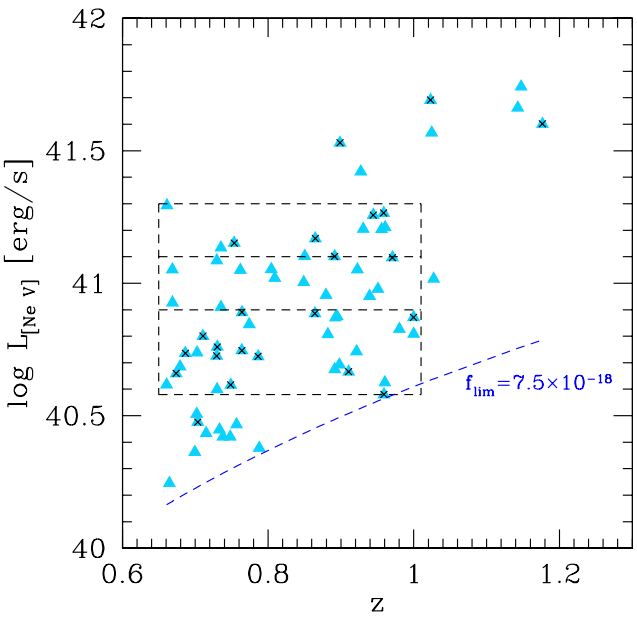

Fig. 5. Distribution of the 69 [Ne V]-selected Type 2 AGN in the [Ne V]line luminosity vs. redshift plane. The 23 objects detected in the X-rays are marked with a cross. The black dashed lines show the boundaries of the three bins used in the computation of the [Ne V] luminosity function. A total of 50 AGN fall in these three luminosity bins. The blue dashed curve shows the [Ne V] flux limit (in units of erg cm^{-2} s^{-1}) of the zCOSMOS survey.

To estimate the fraction of Compton-thick AGN in our sample as most reliably as possible, we divided the sample of 46 sources into two subsamples of similar size: 22 sources with "nominal" X/NeV ratio <30 (hereafter referred to as the "faint" subsample) and 24 sources with "nominal" X/NeV ratio >30 (the "bright" sample), as also described in M13. Stacked X-ray photometry for the former subsample indicates a 1.6σ detection in the rest-frame 2–10 keV band, compared to the 5.8σ detection for the latter subsample. The derived average X/NeV ratios are 3.6 and 36 for the "faint" and "bright" subsample, respectively (shown as filled triangle and square in Fig. 1, respectively).

We then stacked the total sample of 46 X-ray undetected Type 2 AGN, the "faint" and "bright" subsamples; we obtained an average number of 2.6, 1.1 and 3.9 net counts per source, respectively. After verifying that the count distribution of the 46 sources follows a Poisson distribution (see details in M13), we performed 10 000 Monte Carlo runs, each time randomly extracting 46 count values from the Poisson distribution and converting these counts into X-ray fluxes (following the prescriptions reported in Sect. 2). Then these X-ray fluxes were randomly associated with the [Ne V] fluxes to produce X/NeV flux ratios. As a result of the Monte Carlo runs, an average number of 29.4 sources (2.7 rms) were found at X/NeV<15 and are entitled to be considered reliable Compton-thick AGN candidates, bringing the fraction of Compton-thick AGN in the present sample from 13 ± 5%, i.e., 9/69 originally observed at X/NeV < 15, to 43 ± 6% (i.e., 29.4/69, where the reported error is just statistical, and systematic errors related to source selection and stacking analysis are likely much higher). This fraction compares well with XRB synthesis model predictions (≈50%) by Gilli et al. (2007).

As a consistency check, we ran spectral simulations within XSPEC to verify whether the estimated fraction of Compton-thick AGN is consistent with the slope of the stacked spectrum of the 46 X-ray undetected sources ($\Gamma = 0.9 \pm 0.5$). We assumed that the 30 sources with the most stringent limits on the X/NeV ratio are the Compton-thick candidates, whereas the remaining 16 objects are Compton thin. We assumed a pure reflection template spectrum (`pexrav` in XSPEC) for Compton-thick AGN and an absorbed powerlaw for Compton-thin AGN. A soft scattered component was also added in both templates, which mainly contributes at energies below 2 keV rest-frame (see Gilli et al. 2007 and G10 for details). The X-ray flux normalization of each Compton-thin source was obtained by assuming the real source redshift, an intrinsic 2–10 keV rest-frame luminosity of $L_{2-10\ \mathrm{keV}} = 400 \times L_{[\mathrm{NeV}]}$, where $L_{[\mathrm{NeV}]}$ is the measured [Ne V] line luminosity, and a column density estimated through the N_{H} vs. X/NeV model relation of G10. Based on the measured ratio between the median of the X/NeV upper limits of the sources in the "bright" sample and the X/NeV value derived from their stacking, we assumed that each object has an X/NeV ratio a factor of 2 lower than its measured limit. A similar procedure was adopted to normalize the spectra of Compton-thick candidates, based on the "faint" sample. The flux normalization of the `pexrav` spectrum was obtained by assuming that it produces ≈2% of the intrinsic power in the 2–10 keV rest-frame energy band. All spectra were simulated by using an average instrumental response for C-COSMOS sources and by considering for each source its effective exposure in the C-COSMOS mosaic. The 46 spectra were finally co-added using the `addspec` ftool. The simulated stacked spectrum contains ∼110 photons in the 0.5−7 keV band, and a simple powerlaw fit returns a photon index of $\Gamma = 0.40 \pm 0.50$. This value is consistent (within 1σ) with that measured in the real stacked spectrum.

4. The space density of obscured and Compton-thick AGN at $z \approx 0.8$

Based on the standard $1/V_{\mathrm{max}}$ method (Schmidt 1968), we first derived the luminosity function of [Ne V]-selected Type 2 AGN at $z \approx 0.8$ and then the space density of Compton-thick objects among them. The distribution of our sources in the [Ne V] luminosity vs. redshift plane is shown in Fig. 5. For the luminosity function computation we only considered the 50 objects in the redshift range $z = 0.65-1.01$ and in the luminosity range $\log L_{[\mathrm{NeV}]} \approx 40.6-41.3$, which were further subdivided into three

luminosity bins (see Fig. 5). We were forced to choose a single, rather broad redshift range to keep a reasonable number of objects in each luminosity bin. The median redshift of this 50-object sample is $z = 0.83$, and does not vary significantly across the three luminosity bins. The chosen luminosity thresholds guarantee the best completeness level above the [Ne V] flux limit of the zCOSMOS survey ($f_{[\mathrm{NeV}]} > 7.5\times10^{-18}$ erg cm^{-2} s^{-1} at $\approx5\sigma$).

Sources belonging to our sample were first selected to have $I_{AB} < 22.5$ as targets for zCOSMOS optical spectroscopy (see Lilly et al. 2009). Therefore, in the $1/V_{\mathrm{max}}$ computation, we considered as V_{max} the minimum among $V_{[\mathrm{NeV}]}$, $V_{I_{AB}}$ and $V_{z_{\mathrm{max}}}$, where $V_{[\mathrm{NeV}]}$ and $V_{I_{AB}}$ and $V_{z_{\mathrm{max}}}$ are the maximum comoving volumes within which each object would still be included in the sample based on the [Ne V] flux cut, I_{AB} magnitude cut, and our adopted redshift cut ($z = 1.01$), respectively. In addition, a correction that accounts for both the sampling and success rates of zCOSMOS optical spectroscopy needs to be introduced (see, e.g., Bongiorno et al. 2010, hereafter B10). In particular, by defining the target sampling rate (TSR) as the fraction of sources observed in the spectroscopic survey compared to the total number of objects in the parent photometric catalog, and the spectroscopy success rate (SSR) as the fraction of spectroscopically targeted objects for which a secure spectroscopic identification was obtained, trends of TSR and SSR as a function of object magnitude and redshift were determined (Zucca et al. 2009; Bolzonella et al. 2010). A weight can therefore be defined for each object in zCOSMOS as $w_i = 1/(TSR_i \times SSR_i)$. For reference, in our sample w_i ranges from 1.06 to 2.56 and has a mean (median) value of 1.87 (1.93). The [Ne V] luminosity function in the considered redshift bin is therefore given by

$$\Phi(L) = \frac{1}{\Delta \log L} \sum_i \frac{w_i}{V_{\mathrm{max},i}}, \quad (1)$$

and the associated statistical uncertainty is given by (Marshall et al. 1983)

$$\sigma_\phi = \frac{1}{\Delta \log L} \sqrt{\sum_i \frac{w_i^2}{V_{\mathrm{max},i}^2}}. \quad (2)$$

For comparison with literature results, the resulting [Ne V] luminosity function was converted into an [O III] luminosity function using the relation $L_{[\mathrm{OIII}]} = 9.1 \times L_{[\mathrm{NeV}]}$, as derived from objects in our sample that are in the redshift range where both lines can be observed. This relation is also consistent with the average [Ne V]/[O III] ratio derived from the zCOSMOS Type 2 AGN composite spectrum (M13) and from other literature samples (G10).

In Fig. 6 we compare the [O III]-converted luminosity function of our [Ne V]-selected Type 2 AGN at $z = 0.65$–1.01 with that derived by B10 for zCOSMOS Type 2 AGN selected by means of the [O III]/Hβ vs. [O II]/Hβ diagnostic diagram (Lamareille et al. 2004) in a similar redshift range ($z = 0.50$–0.92). With the exception of the datapoint in the faintest luminosity bin, which may suffer from some residual incompleteness (see below for a more complete discussion), the luminosity function of [Ne V]-selected Type 2 AGN at $z \approx 0.8$ appears to be a factor of ~2 higher than that of Type 2 AGN in the same redshift and luminosity range derived by B10. This confirms the result of M13, who showed that a large fraction of Type 2 AGN, selected through their [Ne V] emission, is in fact missed by the optical classification based on the "blue" [O III]/Hβ vs. [O II]/Hβ diagnostic diagram. As also discussed

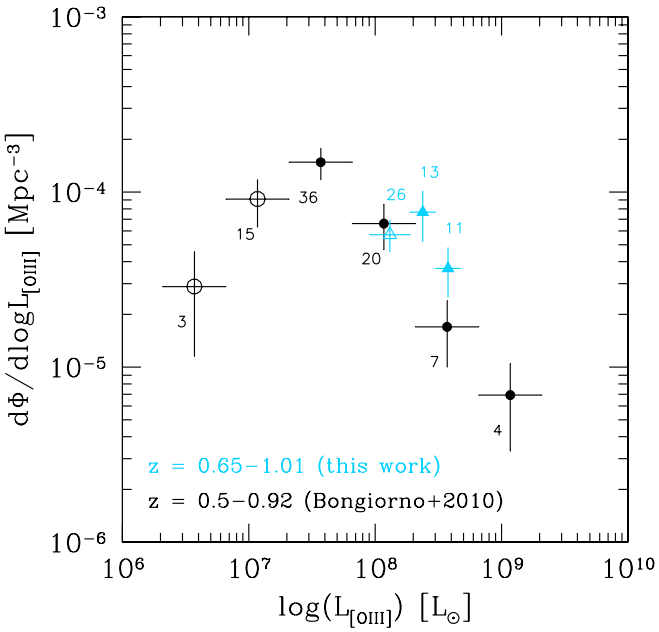

Fig. 6. [O III]-converted luminosity function of [Ne V]-selected Type 2 AGN at $z = 0.65$–1.01 in zCOSMOS (light blue triangles; this work) compared with the [O III] luminosity function of zCOSMOS Type 2 AGN in a similar redshift range selected through the "blue" line diagnostic diagram (black circles; B10). Open symbols highlight those datapoints affected by significant incompleteness (see text and B10). Small numbers indicate how many objects were used to derive each datapoint.

by B10 for their [O III] luminosity function, we note that the drop observed in our luminosity function at the faintest luminosities (see Fig. 6) may result from incompleteness caused by the two-step selection of our sample. In fact, the zCOSMOS magnitude cut at $I = 22.5$ may exclude from the luminosity function objects that would otherwise be in based on their [Ne V] flux. We computed the [Ne V] luminosity at which the luminosity function may suffer from severe incompleteness as follows. Based on the Type 2 AGN composite spectrum of M13, we computed the 3426 Å continuum luminosity corresponding to $I_{AB} = 22.5$ at $z = 1.01$ (the upper redshift boundary adopted in the luminosity function computation). By combining this value with the [Ne V] median EW of the objects included in the luminosity function, we derived the line luminosity at which the magnitude cut would remove approximately half of the objects. This corresponds to $L_{[\mathrm{OIII}],\mathrm{half}} = 1.15 \times 10^8\ L_\odot$ and shows that our luminosity function is largely incomplete in the lowest luminosity bin.

Finally, we combined the two datapoints in our luminosity function that are most complete (i.e., those at $\log L_{[\mathrm{NeV}]} > 40.9$ or, equivalently, $L_{[\mathrm{OIII}]} > 1.9 \times 10^8\ L_\odot$) to evaluate the space density of Compton-thick AGN in our sample. First we computed the space density of the 24 AGN in the range $\Delta\log L_{[\mathrm{NeV}]} = 40.9$–$41.3$ at $z = 0.65$–1.01 (by using Eq. (1) and then multiplying back by the $\Delta\log L$ term), and then we multiplied this density by the fraction of Compton-thick objects f_{Thick} as derived in Sect. 3.2 (i.e., $f_{\mathrm{Thick}} = 0.43$). The resulting space density of Compton-thick AGN at $z = 0.83$ as derived from our sample is then $\Phi_{\mathrm{Thick}} = (9.1 \pm 2.1) \times 10^{-6}$ Mpc^{-3}. To compare this result with the predictions from AGN synthesis models of the XRB and literature results, we converted the [Ne V] luminosity threshold of $\log L_{NeV} > 40.9$ into an X-ray luminosity threshold. In particular, since we are interested in the intrinsic AGN power, we used the relation $\log L_{2-10\ \mathrm{keV}} = 2.6 + \log L_{[\mathrm{NeV}]}$ as derived by G10 for *unobscured* AGN, where $L_{2-10\ \mathrm{keV}}$ is the intrinsic,

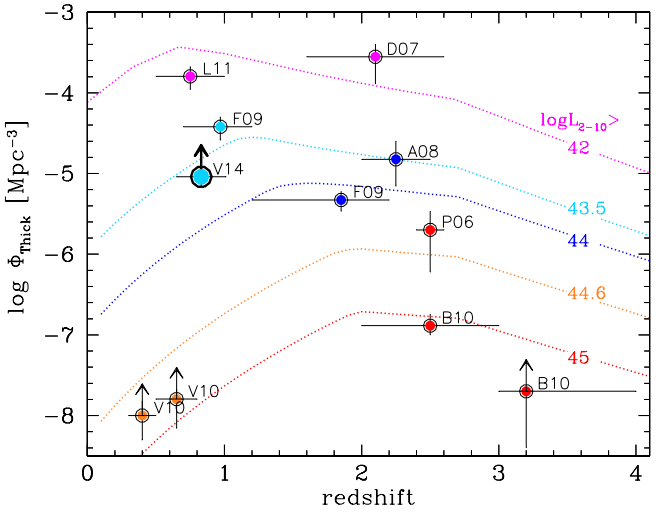

Fig. 7. Space density of Compton-thick AGN samples with different intrinsic 2–10 keV luminosities compared with the XRB model predictions (Gilli et al. 2007). Datapoints have to be compared with the corresponding color curves; luminosity thresholds are as labeled. References to the observed densities, sorted by increasing luminosity threshold, and by increasing redshift for the same luminosity threshold, are as follows: L11: Luo et al. (2011); D07: Daddi et al. (2007b); V14: this work; F09: Fiore et al. (2009); A08: Alexander et al. (2008); V10: Vignali et al. (2010); P06: Polletta et al. (2006); B10: Bauer et al. (2010).

rest-frame 2–10 keV luminosity. The derived space density of Compton-thick AGN at $z = 0.83$ with $\log L_{2-10\,\mathrm{keV}} > 43.5$ is shown in Fig. 7 along with some measurements of the density of Compton-thick AGN in different luminosity and redshift ranges reported by other works and with the expectations from the XRB model of Gilli et al. (2007) (see also Alexander et al. 2011 for an additional estimate at $z \approx 2$; and Della Ceca et al. 2008 and Severgnini et al. 2012 for measurements at $z < 0.06$). Our measurement is in good agreement with both the model expectations for $\log L_{2-10\,\mathrm{keV}} > 43.5$ and the space density measured by Fiore et al. (2009) for objects in a similar redshift and luminosity range selected through their mid-IR excess in their SED. Since, as discussed earlier, even a mild extinction in the NLR can suppress [Ne V] emission, we regard our selection technique for Compton-thick AGN as clean but not complete (see the extended discussion on this issue in M13). This is why we plot our measured space density with an upward arrow in Fig. 7 (see also Vignali et al. 2010 who discuss a similar issue on the space density of [O III]-selected Type 2 AGN at $z \approx 0.3$–0.8).

5. Conclusions

According to XRB synthesis models, a significant fraction of the XRB emission at 20 keV (the so-called "missing XRB") is produced by Seyfert-like Compton-thick objects at $z \approx 0.5$–1.0 and with 2–10 keV intrinsic luminosities $<10^{44}$ erg s^{-1} (see Fig. 2 of Gilli 2013). To this goal, we have selected a sample of 69 Type 2 AGN drawn from the zCOSMOS-Bright Survey on the basis of the presence of the [Ne V]3426 Å emission line at $z = 0.65$–1.20, a reliable tracer of AGN accretion. In this paper we have presented the X-ray properties of these sources (through individual analyses and stacking), and estimated the fraction of Compton-thick AGN on the basis of the X/NeV ratio (see G10). Finally, we have computed the space density of Compton-thick AGN at $z \approx 0.8$ and compared it with previous results and Gilli et al. (2007) XRB model expectations. The main results are as follows:

- Twenty-three of the 69 [Ne V]-selected Type 2 AGN were detected in the *Chandra*-COSMOS observations. Their spectral properties suggest a wide range of absorption, going from limited obscuration for few sources among those with most X-ray photons to heavy obscuration, although formally none of these objects has X/NeV ratio falling in the Compton-thick AGN region.
- Using X-ray stacking analysis for the individually X-ray undetected Type 2 AGN coupled with Monte Carlo simulations provides a fraction of ≈43% of Compton-thick AGN in the sample of 69 [Ne V]-selected Type 2 AGN.
- The derived space density of Compton-thick AGN at $z = 0.83$ is $\Phi_{\mathrm{Thick}} = (9.1 \pm 2.1) \times 10^{-6}$ Mpc^{-3}. This value is in good agreement with XRB model expectations for $\log L_{2-10\,\mathrm{keV}} > 43.5$ AGN and with the previously measured space density for Compton-thick objects in a similar redshift and luminosity range (Fiore et al. 2009).
- The [O III] luminosity function, "converted" from the measured [Ne V] luminosity function, is a factor of ≈ 2 above that computed by B10 for Type 2 AGN selected in the zCOSMOS survey at similar redshifts using the [O III]/Hβ vs. [O II]/Hβ diagnostic diagram. This result indicates that any optical selection method based on spectroscopy and diagnostic diagrams is not complete in finding obscured AGN. Therefore, to search for the most heavily obscured objects, a "panchromatic" observing strategy is the way to go (e.g., Delvecchio et al., in prep.).

Acknowledgements. C.V. thanks M. Bolzonella for useful discussion. Financial contribution from "PRIN–INAF 2011" and "PRIN–INAF 2012" is acknowledged. K.I. thanks support from Spanish Ministerio de Cíencia e Innovacíon (MICINN) through the grant (AYA2010-21782-C03-01).

References

Ajello, M., Alexander, D. M., Greiner, J., et al. 2012, ApJ, 749, 21
Akylas, A., Georgakakis, A., Georgantopoulos, I., Brightman, M., & Nandra, K. 2012, A&A, 546, A98
Alexander, D. M., Smail, I., Bauer, F. E., et al. 2005, Nature, 434, 738
Alexander, D. M., Brandt, W. N., Smail, I., et al. 2008, AJ, 135, 1968
Alexander, D. M., Bauer, F. E., Brandt, W. N., et al. 2011, ApJ, 738, 44
Alexander, D. M., Stern, D., Del Moro, A., et al. 2013, ApJ, 773, 125
Anders, E., & Grevesse, N. 1989, Geochim. Cosmochim. Acta, 53, 197
Arnaud, K. A. 1996 in Astronomical Data Analysis Software and Systems V, ASP Conf. Ser., 101, 17
Avni, Y. 1976, ApJ, 210, 642
Ballantyne, D. R. 2009, ApJ, 698, 1033
Bauer, F. E., Yan, L., Sajina, A., & Alexander, D. M. 2010, ApJ, 710, 212
Beckmann, V., Soldi, S., Ricci, C., et al. 2009, A&A, 505, 417
Bolzonella, M., Kovač, K., Pozzetti, L., et al. 2010, A&A, 524, A76
Bongiorno, A., Mignoli, M., Zamorani, G., et al. 2010, A&A, 510, A56 (B10)
Brightman, M., & Ueda, Y. 2012, MNRAS, 423, 702
Brightman, M., Nandra, K., Salvato, M., et al. 2014, MNRAS, 443, 1999
Broos, P. S., Townsley, L. K., Feigelson, E. D., et al. 2010 ApJ, 714, 1582
Brusa, M., Civano, F., Comastri, A., et al. 2010, ApJ, 716, 348
Brusa, M., Bongiorno, A., Cresci, G., et al. 2014, MNRAS, in press [arXiv:1409.1615]
Buchner, J., Georgakakis, A., Nandra, K., et al. 2014, A&A, 564, A125
Burlon, D., Ajello, M., Greiner, J., et al. 2011, ApJ, 728, 58
Cappelluti, N., Brusa, M., Hasinger, G., et al. 2009, A&A, 497, 635
Cash, W. 1979, ApJ, 228, 939
Castelló-Mor, N., Carrera, F. J., Alonso-Herrero, A., et al. 2013, A&A, 556, A114
Cattaneo, A., Faber, S. M., Binney, J., et al. 2009, Nature, 460, 213
Chartas, G., Brandt, W. N., Gallagher, S. C., & Garmire, G. P. 2002, ApJ, 579, 169
Cicone, C., Maiolino, R., Sturm, E., et al. 2014, A&A, 562, A21

Civano, F., Elvis, M., Brusa, M., et al. 2012, ApJS, 201, 30 (C12)
Comastri, A. 2004, Supermassive Black Holes in the Distant Universe, in Astrophysics and Space Science Library, eds. A. J. Barger (Kluwer), 308, 245
Comastri, A., Ranalli, P., Iwasawa, K., et al. 2011, A&A, 526, L9
Daddi, E., Dickinson, M., Morrison, G., et al. 2007a, ApJ, 670, 156
Daddi, E., Alexander, D. M., Dickinson, M., et al. 2007b, ApJ, 670, 173
Della Ceca, R., Caccianiga, A., Severgnini, P., et al. 2008, A&A, 487, 119
Del Moro, A., Alexander, D. M., Mullaney, J. R., et al. 2013, A&A, 549, A59
Dey, A., Soifer, B. T., Desai, V., et al. 2008, ApJ, 677, 943
Di Matteo, T., Springel, V., & Hernquist, L. 2005, Nature, 433, 604
Donley, J. L., Koekemoer, A. M., Brusa, M., et al. 2012, ApJ, 748, 142
Elvis, M., Civano, F., Vignali, C., et al. 2009, ApJS, 184, 158
Ferrarese, L., & Merritt, D. 2000, ApJ, 539, L9
Feruglio, C., Maiolino, R., Piconcelli, E., et al. 2010, A&A, 518, L155
Feruglio, C., Daddi, E., Fiore, F., et al. 2011, ApJ, 729, L4
Fiore, F., Grazian, A., Santini, P., et al. 2008, ApJ, 672, 94
Fiore, F., Puccetti, S., Brusa, M., et al. 2009, ApJ, 693, 447
Gandhi, P., Horst, H., Smette, A., et al. 2009, A&A, 502, 457
Gebhardt, K., Bender, R., Bower, G., et al. 2000, ApJ, 539, L13
Georgantopoulos, I., Akylas, A., Georgakakis, A., & Rowan-Robinson, M. 2009, A&A, 507, 747
Georgantopoulos, I., Comastri, A., Vignali, C., et al. 2013, A&A, 555, A43
Gilli, R. 2013, Mem. Soc. Astron. It., 84, 647
Gilli, R., Comastri, A., & Hasinger, G. 2007, A&A, 463, 79
Gilli, R., Vignali, C., Mignoli, M., et al. 2010, A&A, 519, A92 (G10)
Gilli, R., Su, J., Norman, C., et al. 2011, ApJ, 730, L28
Gilli, R., Norman, C., Vignali, C., et al. 2014, A&A, 562, A67
Goulding, A. D., Alexander, D. M., Mullaney, J. R., et al. 2011, MNRAS, 411, 1231
Harrison, C. M., Alexander, D. M., Swinbank, A. M., et al. 2012, MNRAS, 426, 1073
Harrison, C. M., Alexander, D. M., Mullaney, J. R., & Swinbank, A. M. 2014, MNRAS, 441, 3306
Hickox, R. C., Jones, C., Forman, W. R., et al. 2009, ApJ, 696, 891
Hopkins, P. F., Hernquist, L., Cox, T. J., & Kereš, D. 2008, ApJS, 175, 356
Houck, J. R., Soifer, B. T., Weedman, D., et al. 2005, ApJ, 622, L105
Jia, J., Ptak, A., Heckman, T., & Zakamska, N. L. 2013, ApJ, 777, 27
Kalberla, P. M. W., Burton, W. B., Hartmann, D., et al. 2005, A&A, 440, 775
Kormendy, J., & Richstone, D. 1995, ARA&A, 33, 581
Iwasawa, K., Gilli, R., Vignali, C., et al. 2012a, A&A, 546, A84
Iwasawa, K., Mainieri, V., Brusa, M., et al. 2012b, A&A, 537, A86
Lacy, M., Storrie-Lombardi, L. J., Sajina, A., et al. 2004, ApJS, 154, 166
Lacy, M., Ridgway, S. E., Gates, E. L., et al. 2013, ApJS, 208, 24
Lamareille, F., Mouhcine, M., Contini, T., Lewis, I., & Maddox, S. 2004, MNRAS, 350, 396
LaMassa, S. M., Heckman, T. M., Ptak, A., et al. 2009, ApJ, 705, 568
Lamastra, A., Bianchi, S., Matt, G., et al. 2009, A&A, 504, 73
Lamastra, A., Menci, N., Fiore, F., et al. 2013, A&A, 559, A56
Lansbury, G. B., Alexander, D. M., Del Moro, A., et al. 2014, ApJ, 785, 17
Lanzuisi, G., Piconcelli, E., Fiore, F., et al. 2009, A&A, 498, 67
Lilly, S.J., Le Févre, O., Renzini, A., et al. 2007, ApJS, 172, 70
Lilly, S.J., Le Brun, V., Maier, C., et al. 2009, ApJS, 184, 218
Luo, B., Brandt, W. N., Xue, Y. Q., et al. 2011, ApJ, 740, 37
Mainieri, V., Hasinger, G., Cappelluti, N., et al. 2007, ApJS, 172, 368
Maiolino, R., Gallerani, S., Neri, R., et al. 2012, MNRAS, 425, L66
Martínez-Sansigre, A., Rawlings, S., Lacy, M., et al. 2005, Nature, 436, 666
Marshall, H. L., Tananbaum, H., Avni, Y., & Zamorani, G. 1983, ApJ, 269, 35
Mateos, S., Alonso-Herrero, A., Carrera, F. J., et al. 2013, MNRAS, 434, 941
Menci, N., Fiore, F., Puccetti, S., & Cavaliere, A. 2008, ApJ, 686, 219
Merloni, A., & Heinz, S. 2013, Evolution of Active Galactic Nuclei, in Planets, Stars and Stellar Systems. Vol. 6: Extragalactic Astronomy and Cosmology, 503 (Springer)
Mignoli, M., Vignali, C., Gilli, R., et al. 2013, A&A, 556, A29 (M13)
Moretti, A., Vattakunnel, S., Tozzi, P., et al. 2012, A&A, 548, A87
Nesvadba, N. P. H., Lehnert, M. D., De Breuck, C., Gilbert, A. M., & van Breugel, W. 2008, A&A, 491, 407
Piconcelli, E., Jimenez-Bailón, E., Guainazzi, M., et al. 2005, A&A, 432, 15
Polletta, M. d. C., Wilkes, B. J., Siana, B., et al. 2006, ApJ, 642, 673
Ptak, A., Zakamska, N. L., Strauss, M. A., et al. 2006, ApJ, 637, 147
Puccetti, S., Vignali, C., Cappelluti, N., et al. 2009, ApJS, 185, 586
Schmidt, M. 1968, ApJ, 151, 393
Scoville, N., Abraham, R.G., Aussel, H., et al. 2007, ApJS, 172, 38
Severgnini, P., Caccianiga, A., & Della Ceca, R. 2012, A&A, 542, A46
Shi, Y., Helou, G., & Armus, L. 2013, ApJ, 777, 6
Silk, J., & Rees, M. J. 1998, A&A, 331, L1
Stern, D., Eisenhardt, P., Gorjian, V., et al. 2005, ApJ, 631, 163
Tombesi, F., Cappi, M., Reeves, J. N., & Braito, V. 2012, MNRAS, 422, L1
Tozzi, P., Gilli, R., Mainieri, V., et al. 2006, A&A, 451, 457
Treister, E., Urry, C. M., & Virani, S. 2009, ApJ, 696, 110
Treister, E., Natarajan, P., Sanders, D. B., et al. 2010, Science, 328, 600
Trouille, L., & Barger, A. J. 2010, ApJ, 722, 212
Tueller, J., Mushotzky, R. F., Barthelmy, S., et al. 2008, ApJ, 681, 113
Vasudevan, R. V., Brandt, W. N., Mushotzky, R. F., et al. 2013, ApJ, 763, 111
Vignali, C. 2014, in Multiwavelength AGN Surveys and Studies, eds. A. Mickaelian & D. Sanders, IAU Sympos., 304, 132
Vignali, C., Alexander, D. M., & Comastri, A. 2006, MNRAS, 373, 321
Vignali, C., Alexander, D. M., Gilli, R., & Pozzi, F. 2010, MNRAS, 404, 48
Villforth, C., Hamann, F., Rosario, D. J., et al. 2014, MNRAS, 439, 3342
Vito, F., Vignali, C., Gilli, R., et al. 2013, MNRAS, 428, 354
Weedman, D. W., Soifer, B. T., Hao, L., et al. 2006, ApJ, 651, 101
Zubovas, K., & King, A. R. 2012, MNRAS, 426, 2751
Zucca, E., Bardelli, S., Bolzonella, M., et al. 2009, A&A, 508, 1217